Hindawi
Journal of Nanomaterials
Volume 2023, Article ID 6675683, 10 pages
https://doi.org/10.1155/2023/6675683

Research Article

The Effects of Ag Nanoislands on the Volatile Threshold-Switching Behaviors of Au/Ag/HfO_2/Ag Nanoislands/Au Devices

Fanlin Long,[1] **Yichuan Zhang**,[1] **Zhaozhu Qu**,[1] **Peiwen Lv**,[2] **and Baolin Zhang**[1]

[1]*Key Laboratory of New Processing Technology for Nonferrous Metal and Materials, Ministry of Education, Guangxi Key Laboratory of Optical and Electronic Materials and Devices, College of Materials Science and Engineering, Guilin University of Technology, Jian Gan Road 12, Guilin 541004, China*
[2]*Fujian Institute of Research on the Structure of Matter, Chinese Academy of Sciences, Fuzhou 350000, China*

Correspondence should be addressed to Baolin Zhang; baolinzhang@ymail.com

Received 24 November 2022; Revised 6 April 2023; Accepted 8 April 2023; Published 6 May 2023

Academic Editor: Jianbo Yin

Volatile threshold-switching (TS) devices have been used as selectors and to simulate neurons in neural networks. It is necessary to find new ways to improve their performance. The randomness of conductive filament (CF) growth and the endurance of the devices are urgent issues at present. Here, we explored embedded Ag nanoislands (NIs) in HfO_2-based TS devices to limit the position of the CF and facilitate its growth at the same time. The Au/Ag(2 nm)/HfO_2(4 nm)/Ag NIs/Au volatile TS devices exhibited forming-free characteristics with improved endurance compared with the devices without Ag NIs, which was ascribed to the enhanced localization of the electrical field and increased oxygen vacancies in HfO_2 induced by the Ag NIs. A mechanism was proposed to explain the volatile TS behaviors of the devices. The Ag NIs and the thickness of the HfO_2 layers played key roles in whether the devices required forming. This work shows that the use of metal NIs is an effective and convenient way to improve the performance of TS devices.

1. Introduction

Computer systems based on the von Neumann architecture, where storage and computation are separated, face bottlenecks in big data processing [1, 2]. Brain-inspired neural networks have the potential to process information with much lower power consumption than conventional processors and to move the control from data centers to edge devices. Memristors can be used to realize these neural networks as the basic elements to reduce the power consumption and the footprint of the circuits [3]. According to the resistive state retention characteristics of memristors, they can be divided into volatile threshold-switching (TS) devices [4, 5] and nonvolatile memory devices [6, 7]. The volatile TS devices can leverage their large ON/OFF ratios and low-leakage currents to be used as selectors or combine simple external circuits to simulate partial neuronal functions [8, 9]. When combined with external circuits to simulate neuronal function, the volatile TS devices need to be connected in parallel with an external capacitor and then in series with a resistor [10, 11]. The pulse signal generated by the whole circuit can be encoded and used for neuromorphic network calculations [12, 13]. Recently, it has been proven that volatile TS devices can simulate Hodgkin–Huxley and leaky integrate-and-fire neurons [14–16]. To simulate neurons, volatile TS devices with mechanisms of electrochemical metallization (ECM), metal–insulator transition (MIT), or the chalcogenide phase change materials (PCMs) are explored [17–21]. MIT- or PCMs-based volatile TS devices are based on the transformation between the high-resistance phase and the low-resistance phase of the dielectric layer of the devices [22]. Although they have an extremely fast switching speed, there are still many problems. First, the thermal cross talk of large-scale integration can make the whole circuit unstable [23]. Second, the transition temperature of the MIT-based material is too low, requiring a harsh working environment. Third, the devices have a high-leakage current in the off state (I_{OFF}) [24–28]. The working principle of ECM-based volatile TS devices is that with an applied bias voltage, active atoms such as Cu or Ag are oxidized to metal ions at the positive

electrode and diffuse toward the negative electrode, after being reduced by the electrons encountered, the metal atoms finally form a conductive filament (CF) [16, 29]. The resistance of the device changes from the HRS to the LRS, and when the bias voltage is removed or reduced to become insufficient to maintain the CF, the CF will spontaneously break, and the resistance of the device returns to the HRS. At present, there are still some challenges for ECM-based volatile TS devices, such as poor threshold voltage uniformity and endurance. To obtain high performance of the volatile TS devices, relying on patterned controllable Ag nanodots prepared by e-beam lithography, the randomness of CF growth was decreased and the threshold voltage uniformity was improved in HfO_2-based TS [20], but the complicated process limited the application. Forming has a heavy impact on the performance of volatile TS devices. The initial forming process can usually lead to large parameter variations, poor endurance, and even worse [30], induce permanent damage to themselves due to the applications of large voltages and currents because excessive metal ions are injected into the dielectric layer so that a stable CF is formed during the forming process [30, 31]. Forming-free HfO_2-based volatile TS devices were prepared by rapid thermal processing to eliminate the forming process and improve endurance [32], however, the diffusion of active metals was random and uncontrollable in the rapid thermal process, which is not the best choice for improving the integrated performance of volatile TS devices.

In this work, we explored Ag nanoislands (NIs) in Au/Ag (2 nm)/HfO_2(4 nm)/Ag NIs/Au volatile TS devices to improve their electrical performance. It was found that the introduction of Ag NIs made the devices exhibit forming-free TS behavior. The endurance of the devices was improved as compared with that of the devices without Ag NIs. This work demonstrated an effective and convenient method by using metal NIs to eliminate forming, decrease the TS voltage and increase the endurance of ECM-based volatile TS devices.

2. Materials and Methods

2.1. Preparation of the Devices. Figure 1(a) shows the schematic diagram elucidating a device in the cross-point of the bottom electrode (BE) and top electrode (TE). Figure 1(b) shows the SEM vertical view of the cross-point structure. An ~300 nm thick layer of SiO_2 was grown on a cleaned 2-inch wafer using plasma-enhanced chemical vapor deposition. The pattern of the BE (Figure 1(b)) was formed by photolithography, and 100 nm thick Ti and 100 nm thick Au were successively deposited as the BE using magnetron sputtering. Ag NIs with a thickness of 2 nm were prepared using an ultrathin anodic aluminum oxide (AAO) template and electron beam evaporation deposition [33]. In this experiment, the AAO template was used as a mask with a hole diameter of 40 nm, hole–hole center distance of 100 nm, and thickness of 200 nm. After cleaning, the HfO_2 layer was deposited using plasma-enhanced atomic layer deposition (PEALD) at 280°C using oxygen plasma and a tetrakis(ethylmethylamino)hafnium precursor. The pattern of the TE (Figure 1(b)) was formed by photolithography, and 2 nm thick Ag and 100 nm thick Au protective layers were deposited sequentially as the TE using magnetron sputtering.

2.2. Characterization Methods. Scanning electron microscopy (SEM, Gemini SEM 300, Germany and Hitachi S-4800, Japan) was used to characterize the morphology of Ag NIs and the fracture surface. Grazing incidence X-ray diffraction (GIXRD, Smartlab 9 kW, Rigaku, Japan) with the incident angle of 0.5° and the copper target was used to analyze the crystal structure of the HfO_2 film. X-ray photoelectron spectroscopy (XPS, Thermo Fisher K alpha, Thermo Fisher Scientific, USA) was used to analyze the element valence and composition of the HfO_2 film, and the diameter of the X-ray beam was ~100 μm, which was focused on the HfO_2 film surface (red circle in Figure 1(b)). For depth analysis, argon ion bombardment was used to etch the HfO_2 film. The data were analyzed using the computer software Avantage, and the peaks were calibrated by the C 1 s peak at 284.8 eV. The electrical properties of the devices were measured by using a semiconductor parameter meter (Keithley 4200-SCS, KEITHLEY, Cleveland, USA) and a source meter (Keithley 2636B, KEITHLEY, Cleveland, USA). Two 5 μm diameter tungsten-plated steel probes were connected to the TE and BE.

3. Results

3.1. XRD and SEM Analyses. As shown in Figure 1(b), it can be measured that the linewidths of the BE and TE are ~21.1 and 20.8 μm, respectively, so the area of the cross-point is ~438.9 μm^2, which is consistent with the designed size. Figure 1(c) shows the SEM morphology of the Ag NIs, which were from the same batch of devices but without deposition of the hafnium oxide layer and TE. The Ag NIs prepared with the AAO template and electron beam evaporation deposition of Ag have a diameter of ~45 nm, and the center distance between two Ag NIs is ~103 nm, so it can be estimated that the average number of Ag NIs per square micron is ~109. The layered structure of HfO_2(4 nm)/Ag NIs/Au (area outside the cross-point) observed by SEM is shown in Figure 1(d). Figure 1(e) shows the GIXRD spectrum of Au/Ag(2 nm)/HfO_2(4 nm)/Ag NIs/Au device. The hafnium oxide (JCPDS#34-0104) prepared by PEALD has one feature diffraction peak belonging to the $(\bar{2}21)$ crystal plane [34, 35], and strong feature diffraction peaks were not observed possibly due to the special crystal texture of the HfO_2 deposited.

3.2. Volatile TS Behavior of the Devices. To analyze the TS behaviors of the devices, the *I–V* curves of the Au/Ag(2 nm)/HfO_2 (4 nm)/Ag NIs/Au device were measured by a Keithley 4200-SCS (Figure 2(a)). The device abruptly switched from the high-resistance state (HRS) to the low-resistance state (LRS) at a V_{th} of ≈−0.04 V when the negative voltages were swept from 0 to −0.5 V (blue arrows in Figure 2(a)); the device abruptly switched from the HRS to the LRS at a V_{th} of ≈0.03 V, when the positive voltages were swept from 0 to 0.5 V (green arrows in Figure 2(a)). The electrical states of the

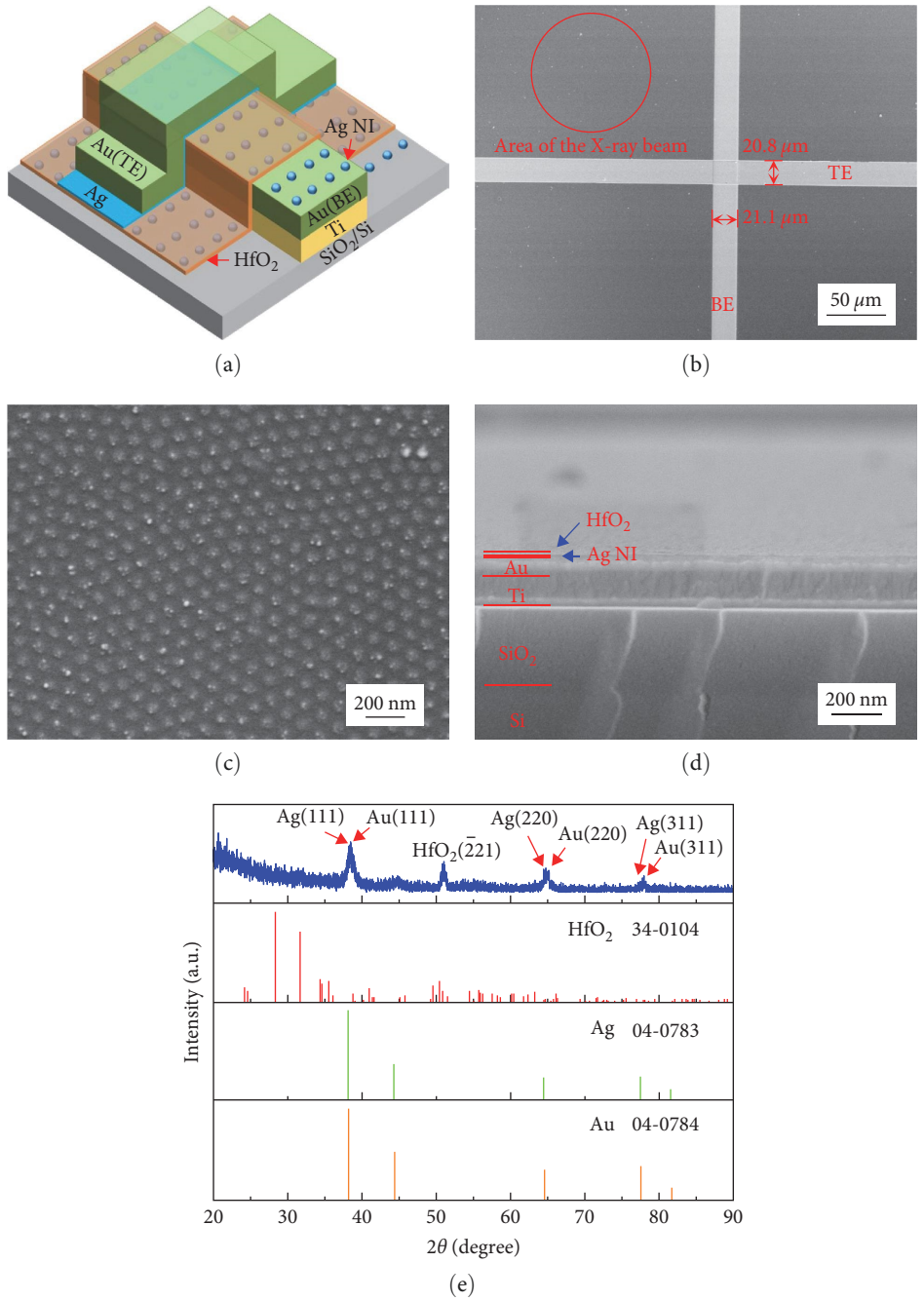

FIGURE 1: (a) Schematic diagram of the Au/Ag(2 nm)/HfO_2 (4 nm)/Ag NIs/Au device, (b) SEM image of the cross-point structure, (c) SEM image of Ag NIs, (d) SEM image of the fracture surface of the wafer with BE (without TE), and (e) GIXRD pattern of the device.

device returned to the HRS when the voltages were reduced to ~0 V, showing typical volatile TS behaviors. The volatile TS behaviors could be repeated for ~80 cycles under a compliance current (I_{CC}) of 10 μA, and then the device failed by remaining in the LRS. Figure 2(d) shows the cumulative probability distributions of cycle to cycle and device to device in the positive and negative threshold voltages of the Au/Ag (2 nm)/HfO_2(4 nm)/Ag NIs/Au devices. The positive threshold voltage distribution ranged from 0.01 to 0.08 V, and the negative threshold voltage distribution ranged from −0.02 to −0.08 V. This was consistent with the fact that NIs could greatly decrease the threshold voltages [36].

To perform comparative studies on the effect of Ag NIs on volatile TS behaviors, we prepared Au/Ag(2 nm)/HfO_2(4 nm)/Ag(2 nm)/Au device with a Ag layer instead of Ag NIs and Au/Ag(2 nm)/HfO_2(6 nm)/Ag NIs/Au device (with a different thickness of HfO_2). Figures 2(b) and 2(c) show the volatile I–V curves of Au/Ag(2 nm)/HfO_2(4 nm)/Ag(2 nm)/Au and Au/Ag(2 nm)/HfO_2 (6 nm)/Ag NIs/Au devices, respectively. The devices needed forming voltages of −2.85 and −5.48 V under a I_{CC} of 100 μA to become operational, respectively, then the changing from the HRS to the LRS of the electrical state of the volatile devices occurred at a V_{th} of 2.11 and 2.41 V when the voltages

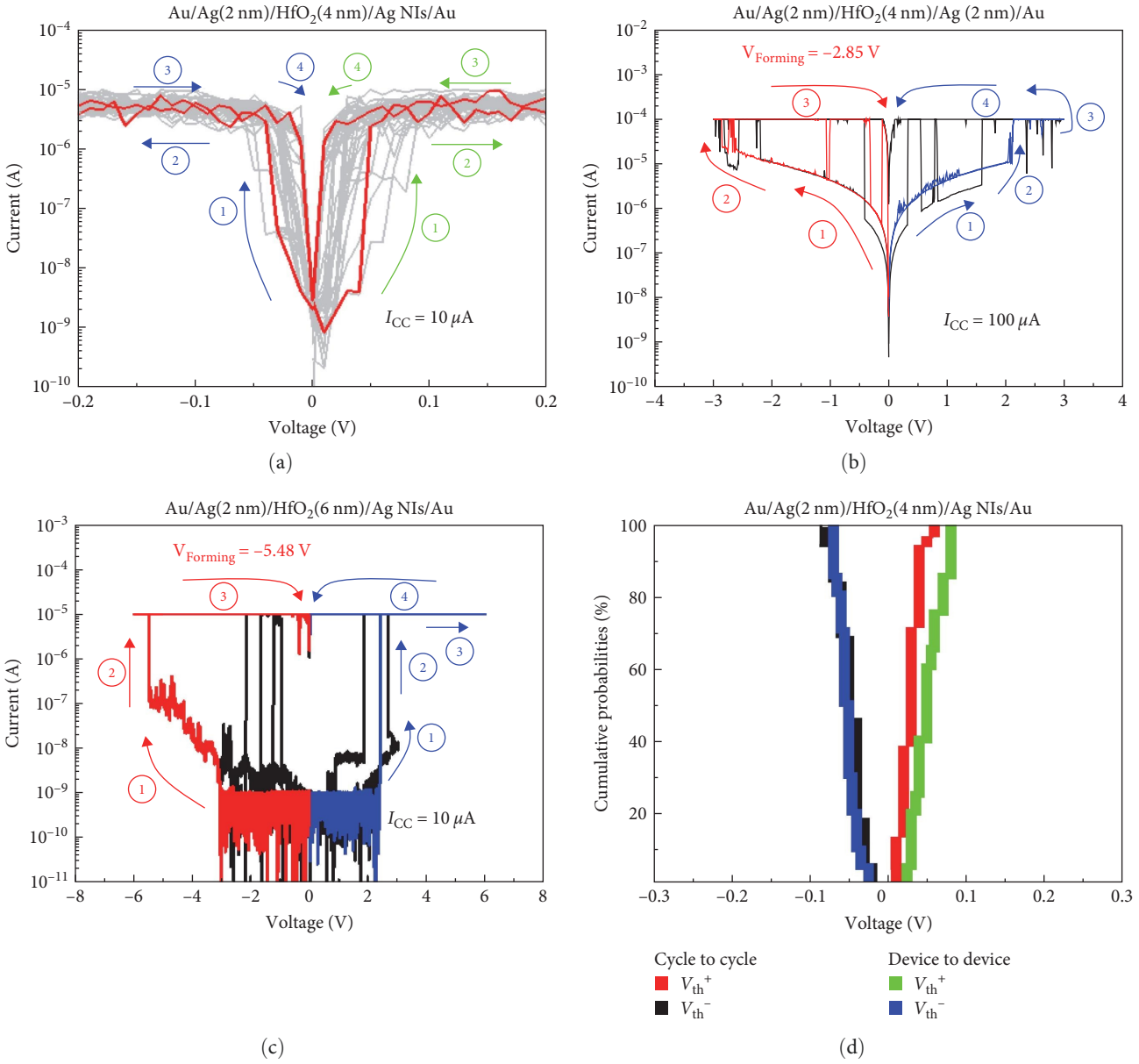

FIGURE 2: (a) Typical volatile *I–V* curves of the Au/Ag(2 nm)/HfO_2(4 nm)/Ag NIs/Au device with 80 cycles of DC voltage sweeps, (b) typical volatile *I–V* curves of the Au/Ag(2 nm)/HfO_2(4 nm)/Ag(2 nm)/Au device with several sweeps, (c) typical volatile *I–V* curves of the Au/Ag (2 nm)/HfO_2(6 nm)/Ag NIs/Au device with several sweeps, and (d) cumulative probabilities of V_{th}^+ and V_{th}^- of the Au/Ag(2 nm)/HfO_2(4 nm)/Ag NIs/Au devices.

were swept from 0 to 3 V (the blue curve in Figures 2(b) and 2(c)), respectively. When the voltages were reduced to ~0 V, the electrical states of the volatile devices changed from the LRS to the HRS (volatile TS behaviors). However, these volatile TS behaviors could be repeated only several times, after which the volatile TS devices failed by remaining in the LRS, and the TS behaviors of the devices also could be repeated only several times under the I_{CC} of 1 and 10 mA, after the forming process (Figure S1(a)–S1(c)).

We further investigated the endurances of the devices under voltage pulses. All devices were measured by a Keithley 2636B instrument. Before the pulse measurements, the Au/Ag (2 nm)/HfO_2(4 nm)/Ag(2 nm) /Au devices and Au/Ag(2 nm)/HfO_2 (6 nm)/Ag NIs/Au devices were electroformed by voltage sweeping from 0 to −3 V and 0 to −6 V, respectively. The LRS of the devices were read at a pulse (5 V, 200 μs), the HRS of the devices were read at a pulse (0.01 V, 200 μs) after the 0 V lasted for 600 μs (delay time for relaxation) (Figure 3(a)–3(c)). The LRS and HRS of Au/Ag(2 nm)/HfO_2(4 nm)/Ag NIs/Au device could still be read out after 5,000 cycles (Figure 3(a)). For the Au/Ag(2 nm)/HfO_2(4 nm)/Ag(2 nm)/Au device and Au/Ag (2 nm)/HfO_2(6 nm)/Ag NIs/Au devices, the HRS could not be effectively read out after about 55 cycles (in Figure 3(b)) and 500 cycles (in Figure 3(c)), respectively.

These comparison results show that the Au/Ag(2 nm)/HfO_2(4 nm)/Ag NIs/Au devices did not need an initial

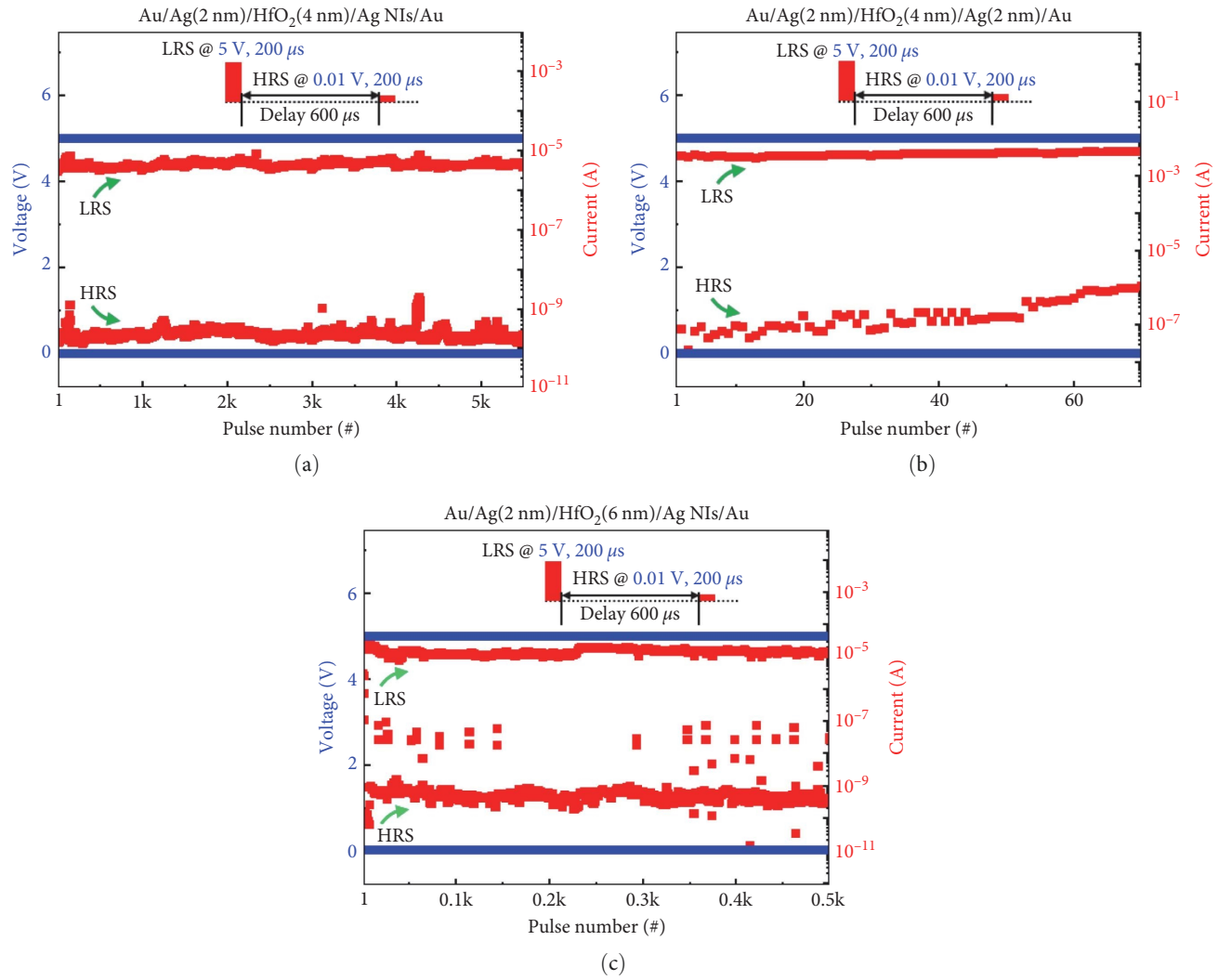

FIGURE 3: The pulse measurements of the Au/Ag(2 nm)/HfO_2(4 nm)/Ag NIs/Au device (a), the Au/Ag(2 nm)/HfO_2(4 nm)/Ag(2 nm)/Au device (b), and the Au/Ag(2 nm)/HfO_2(6 nm)/Ag NIs/Au device (c).

forming process, and the devices had relatively high endurance. The devices prepared with the Ag nanodots on top of the hafnium oxide layer have been reported, but the devices needed a rapid thermal processing at 500°C to eliminate the forming process [32]. We differently used embedded Ag NIs, which were embedded below the hafnium oxide layer in our devices that did not require the forming process in their pristine state. The Au/Ag(2 nm)/HfO_2(4 nm)/Ag(2 nm)/Au and Au/Ag(2 nm)/HfO_2(6 nm)/Ag NIs/Au devices needed forming, and they had much poor endurances. This indicated that the Ag NIs and the thickness of the hafnium oxide layer played a key role in the volatile-switching behaviors of the TS devices.

3.3. X-Ray Photoelectron Analysis. The computer software Avantage was used to analyze the XPS peaks with fitting by Gaussian and Fourier methods. Figure 4(a) shows the full XPS spectra of HfO_2 on SiO_2/Si (the XPS measurement was located on HfO_2 that was directly deposited on SiO_2/Si) and HfO_2 on Ag NIs/SiO_2/Si (the XPS measurement was located on the red circle area as shown in Figure 1(b), and there were Ag NIs underneath). Figure 4(b) shows the O 1 s feature peaks of HfO_2 on SiO_2/Si and on Ag NIs/SiO_2/Si at the surfaces.

We performed argon ions etching on the HfO_2 layer and used XPS to analyze the distribution of oxygen at different depths in HfO_2 on SiO_2/Si and in HfO_2 on Ag NIs/SiO_2/Si. Figure 4(c) shows the O 1 s feature peaks of HfO_2 on SiO_2/Si after the HfO_2 layer was etched by argon ions for 7 and 14 s. Figure 4(d) shows the O 1 s feature peaks of HfO_2 on Ag NIs/SiO_2/Si after the HfO_2 layer was etched by argon ions for 7 and 14 s. From the full XPS spectra obtained after etching time of 7 (Figure 4(e)) and 14 s (Figure 4(f)), the peaks of Hf 4 f in the full XPS spectrum indicate that the etching was performed on hafnium oxide layers, and the characteristic absorption peak of Ag 3d orbit could be detected which was from the Ag under the HfO_2. The peaks located at ~530 and 532 eV correspond to lattice oxygen and nonlattice oxygen, respectively [37]. The percentages of nonlattice oxygen in HfO_2 on SiO_2/Si and in HfO_2 on Ag NIs/SiO_2/Si at different

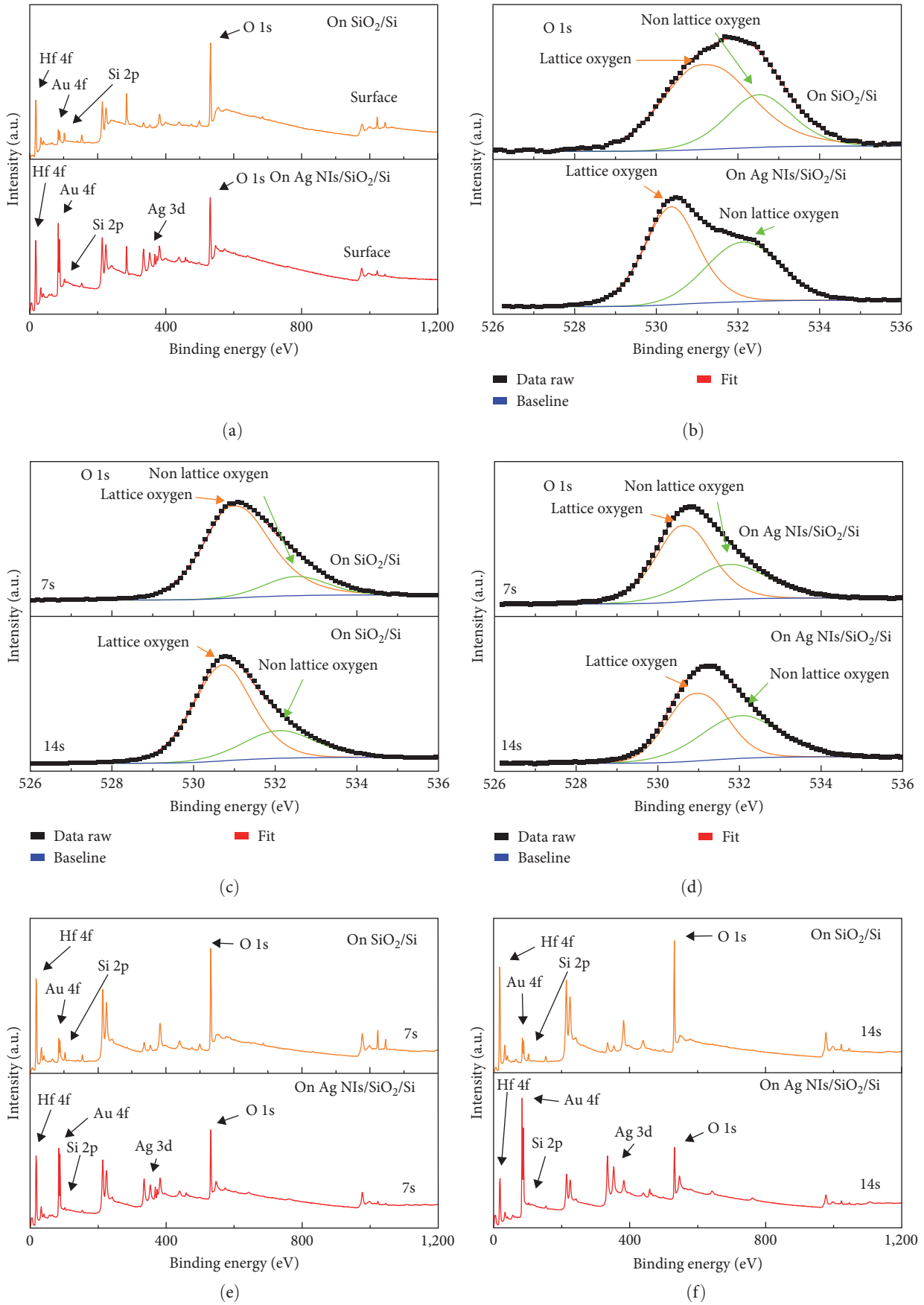

Figure 4: (a) XPS full spectra of HfO_2 on SiO_2/Si and HfO_2 on Ag NIs/SiO_2/Si at the surfaces, (b) the O 1 s feature peaks of HfO_2 on SiO_2/Si and HfO_2 on Ag NIs/SiO_2/Si at the surfaces, (c), (d) the O 1 s feature peaks of HfO_2 on SiO_2/Si and on Ag NIs/SiO_2/Si after etching for 7 and 14 s, respectively, and (e), (f) XPS full spectra of HfO_2 on SiO_2/Si and on Ag NIs/SiO_2/Si after etching for 7 and 14 s, respectively.

Table 1: The percentages of nonlattice oxygens of HfO_2 on SiO_2/Si and on Ag NIs/SiO_2/Si after different etching time.

	Nonlattice oxygens in HfO_2 on SiO_2/Si (%)	Nonlattice oxygens in HfO_2 on Ag NIs/SiO_2/Si (%)
Etching for 0 s (surface)	31.13	44.51
Etching for 7 s	25.03	39.00
Etching for 14 s	25.77	46.06

etching time are listed in Table 1. The high proportion of nonlattice oxygen at the surface of HfO_2 might be due to the contribution of adsorbed oxygen on the surface [38]. The amount of nonlattice oxygen decreased at first in HfO_2 of the two devices after etching for 7 s. However, the amount of nonlattice oxygen significantly increased in HfO_2 on Ag NIs/SiO_2/Si after etching for 14 s. It can be inferred that the presence of Ag NIs led to a high concentration of oxygen vacancies that contribute to nonlattice oxygen in HfO_2 near the Ag NIs [39], which might be attributed to the reaction between the active metal NIs and HfO_2 [33, 36].

4. Discussion

4.1. Mechanism for the Volatile TS Behaviors of the Au/Ag(2 nm)/HfO_2(4 nm)/Ag NIs/Au Device. The Ag ions ($Ag \longrightarrow Ag^+ + e^-$) in the top Ag layer first diffused toward the HfO_2 layer when a positive voltage bias was applied to the TE [40]. Because the diffusion barrier of Ag ions in HfO_2 is higher than that in HfO_x, the diffusion rate of Ag ions in HfO_2 is slower than that in HfO_x [41–43], thus, in HfO_2-based switching devices, it is supposed that the Ag ions were reduced to Ag atoms ($Ag^+ + e^- \longrightarrow Ag$) before arriving at the BE, so the Ag CF most likely grew from near the top Ag layer [43, 44]. In the present work, because the Ag NIs had a tip charge effect, i.e., an enhanced localization of the electric field (ΔE_1) induced by the accumulated electrons (Figure 5(a)) could be formed at the tip of the NIs [33, 36], the Ag ions diffused faster above the tip of the Ag NIs along the electric field, the reduced Ag formed a CF faster at this position. A preferential CF could be formed under a low bias of ~0.03 V (Figure 2(a)). The Au/Ag(2 nm)/HfO_2(4 nm)/Ag NIs/Au device did not require an initial forming process. After the Ag CF formed, the electrical state of the volatile device switched from the HRS to the LRS (Figures 2(a) and 5(a)). According to the Gibbs–Thomson effect, the instability of the atoms on the fiber surface (Ag CF) would be increased [45], and the Ag CF formed under a I_{CC} of 10 μA was unstable after the voltage bias decreasing because of the Rayleigh instability, the cylindrical-shaped structure of the Ag CF tended to break up easily to minimize surface energy [41, 46]. Therefore, when the voltage bias was reduced to ~0 V, the CF instantly dissolved, and the electrical state of the volatile device returned to the HRS (Figures 2(a) and 5(b)).

When a negative voltage was applied to the TE, the Ag ions diffused from the Ag NIs to the TE, which could be accelerated by the oxygen vacancies [41] formed near the Ag NIs (Table 1). Similarly, the Ag ions were rapidly reduced to Ag atoms near the tip of the Ag NIs under the enhanced localization of the electric field (ΔE_2) induced by the accumulated Ag ions at the tip of the Ag NIs (Figure 5(c)). The Ag cluster grew and extended upward from the tip of the Ag NIs, and a preferential Ag CF was formed with a low bias of ~−0.04 V (Figure 5(c)). The electrical state of the volatile device switched from the HRS to the LRS (Figure 2(a)). The CF channel formed under an I_{CC} of 10 μA was unstable after the voltage bias decreasing, when the voltage bias was reduced to ~0 V, the CF instantly dissolved, and the electrical state of the volatile device returned to the HRS (Figures 2(a) and 5(d)).

The XPS analyses (Figure 4(d) and Table 1) show that the Ag NIs led to higher oxygen vacancy concentrations in the HfO_2 layer near the Ag NIs (Figure 5). The oxygen-vacancy defects might promote Ag ion diffusion because of the low-diffusion barrier, which further promoted the formation of conductive channels [41]. The oxygen vacancies in the HfO_2 layer also might participate in the formation of the CF channel, so the CF might consist of oxygen vacancies and Ag atoms [47].

For the Au/Ag(2 nm)/HfO_2(4 nm)/Ag(2 nm)/Au device (without Ag NIs), the Ag CF might form anywhere through a competing CF formation process. The device needed a forming process to form the CF at −2.85 V, and the positive and negative threshold voltages of the devices had a large variation (Figure 2(b)) from 0.33 to 2.12 V and from −0.8 to −2.2 V, respectively.

4.2. Endurance of HfO_2-Based Volatile TS Devices. From the electrical performances evaluated by DC voltage cycle sweeping, it can be found that the volatile TS behaviors of the Au/Ag (2 nm)/HfO_2(4 nm)/Ag NIs/Au device, which did not need a forming process, could be repeated 80 times (Figure 2(a)). The Au/Ag(2 nm)/HfO_2(4 nm)/Ag (2 nm)/Au device (using a Ag layer instead of Ag NIs) and Au/Ag(2 nm)/HfO_2(6 nm)/Ag NIs/Au devices (the thickness of the HfO_2 layer increased to 6 nm) needed forming processes, and the volatile TS behaviors for these devices could be only repeated few times (Figures 2(b) and 2(c)). Under the voltage pulse measurement, the LRS and HRS of the Au/Ag(2 nm)/HfO_2(4 nm)/Ag NIs/Au device were read out over 5,000 cycles (Figure 3(a)); however, the HRS could not be effectively read out after about 55 cycles (Figure 3(b)) and 500 cycles (Figure 3(c)) for the Au/Ag (2 nm)/HfO_2(4 nm)/Ag(2 nm)/Au device and Au/Ag(2 nm)/HfO_2(6 nm)/Ag NIs/Au device after the forming process, respectively. This implies that the forming process affects the endurance of the devices greatly, this is because the forming process might result in the excessive injection of Ag in the dielectric layer, leading to a stable Ag CF so that the electrical

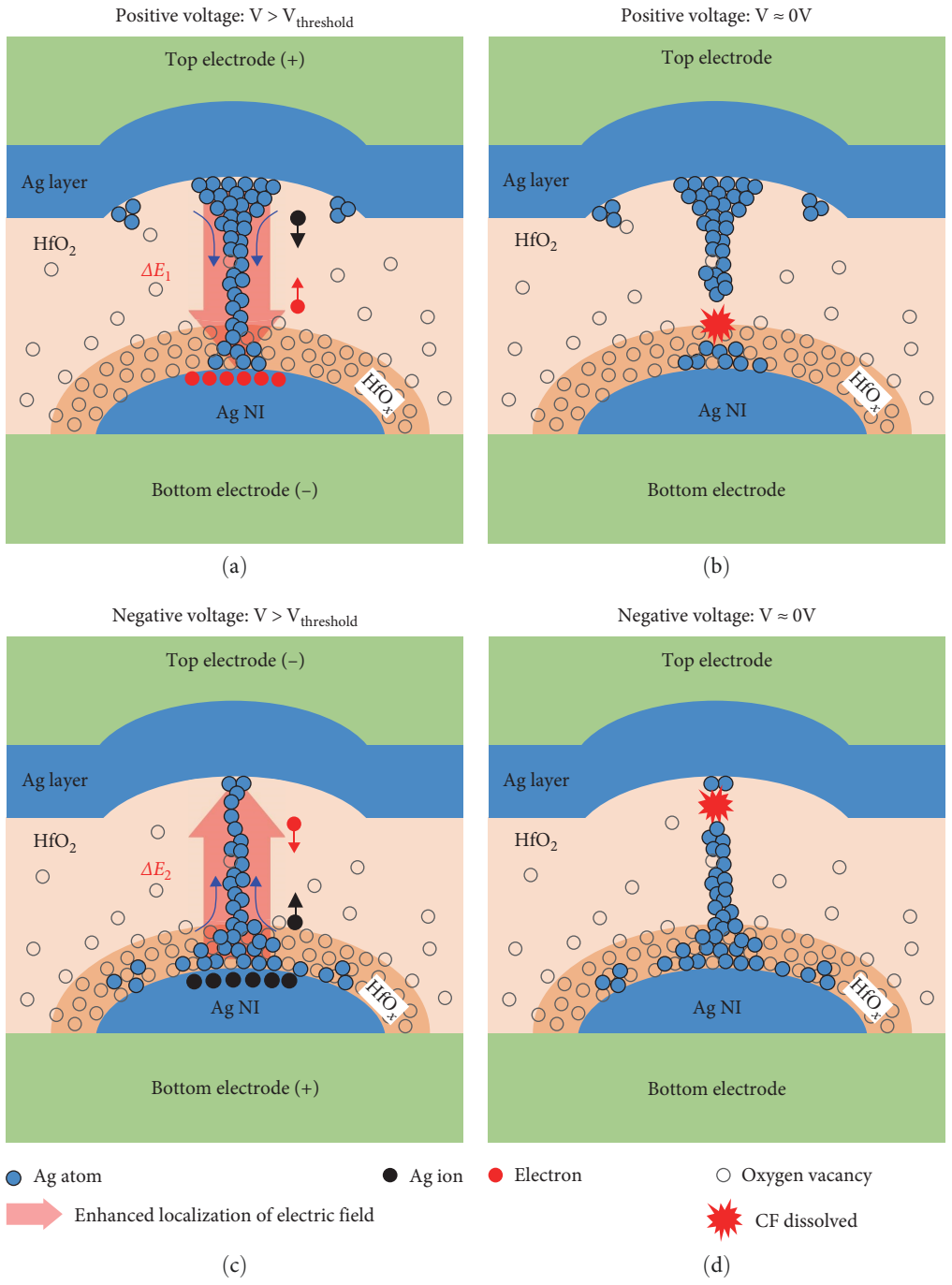

Figure 5: (a) When the positive voltage was applied to the TE, the CF grew from the top Ag layer to bottom to form a conduction channel facilitated by the accumulated electrons-enhanced localization of electric field (ΔE_1) at the tip of Ag NIs, (b) the CF dissolved under the positive voltage of ~0 V, (c) when the negative voltage was applied to the TE, the CF grew from the Ag NI to the Ag layer and form a conduction channel facilitated by the accumulated Ag ions-enhanced localization of electric field (ΔE_2) at the tip of Ag NIs, and (d) the CF dissolved under the negative voltage of ~0 V.

state of the devices no longer exhibited volatile TS behavior because the devices failed by remaining in the LRS, and therefore leading to a poor endurance [38, 48, 49].

The Ag NIs and the thickness of the HfO_2 layers played key roles in whether the devices needed forming, and a forming-free process could avoid excessive Ag injection into the HfO_2 layers, thus improving the endurance of HfO_2-based volatile TS devices. It can be concluded that limiting the excessive injection of Ag into the switching layer would be an effective method to increase the devices endurance.

5. Conclusion

By a comparison study, it has been demonstrated that the Au/Ag(2 nm)/HfO_2(4 nm)/Ag NIs/Au volatile TS devices

exhibited forming-free characteristics with increased endurance and low-threshold voltages. These effects can be ascribed to the enhanced localization of the electric field at the tip of the Ag NIs, which were conveniently embedded into the devices with the help of an ultrathin AAO template. The Ag NIs and the thickness of the HfO_2 layer played key roles in whether the devices needed forming. The forming-free Au/Ag (2 nm)/HfO_2(4 nm)/Ag NIs/Au device could avoid excessive Ag injection into the HfO_2 layers and attain high endurance. It can be expected that the effective and convenient NI strategy can be used to further improve the performance of other TS devices.

Data Availability

In our manuscript, we have provided supporting information as a word document, applied for Section 3.2.

Conflicts of Interest

The authors declare that they have no conflicts of interest.

Authors' Contributions

Fanlin Long was responsible for investigation, writing the original draft, and review and editing. Yichuang Zhang was responsible for formal analysis, writing the original draft, and review and editing. Zhaozhu Qu was responsible for methodology and formal analysis. Peiwen Lv was responsible for methodology, data curation, and formal analysis. Baolin Zhang was responsible for conceptualization, supervision, writing the original draft, and review and editing.

Acknowledgments

This work was supported by the National Natural Science Foundation of China (52162022), the Guangxi Natural Science Foundation (2021JJA160015), Open Fund of Key Laboratory of New Processing Technology for Nonferrous Metal & Materials, Guilin University of Technology, Ministry of Education (19AA-1, 20KF-29).

Supplementary Materials

Figure S1: (a) The *I–V* curves of the Au/Ag(2 nm)/HfO_2(4 nm)/Ag (2 nm)/Au device under the compliance currents of 1 mA (red and blue curves) and 10 mA (green curves). (b) The *I–V* curves of the Au/Ag(2 nm)/HfO_2(6 nm)/Ag NIs/Au device under the compliance currents of 1 mA. (c) The *I–V* curves of the Au/Ag(2 nm)/HfO_2(6 nm)/Ag NIs/Au device under the compliance currents of 10 mA. Figure S2: The SEM image of the Ag film prepared by electron beam evaporation deposition. (*Supplementary Materials*)

References

[1] F. Ma, Y. Zhu, Z. Xu et al., "Optoelectronic perovskite synapses for neuromorphic computing," *Advanced Functional Materials*, vol. 30, no. 11, Article ID 1908901, 2020.

[2] X. Hou, H. Chen, Z. Zhang, S. Wang, and P. Zhou, "2D atomic crystals: a promising solution for next-generation data storage," *Advanced Electronic Materials*, vol. 5, no. 9, Article ID 1800944, 2019.

[3] D. V. Christensen, R. Dittmann, B. Linares-Barranco et al., "2022 roadmap on neuromorphic computing and engineering," *Neuromorphic Computing and Engineering*, vol. 2, no. 2, Article ID 022501, 2022.

[4] H. Abbas, Y. Abbas, G. Hassan et al., "The coexistence of threshold and memory switching characteristics of ALD HfO_2 memristor synaptic arrays for energy-efficient neuromorphic computing," *Nanoscale*, vol. 12, no. 26, pp. 14120–14134, 2020.

[5] A. S. Sokolov, M. Ali, R. Riaz, Y. Abbas, M. J. Ko, and C. Choi, "Silver-adapted diffusive memristor based on organic nitrogen-doped graphene oxide quantum dots (N-GOQDs) for artificial biosynapse applications," *Advanced Functional Materials*, vol. 29, no. 18, Article ID 1807504, 2019.

[6] H. Abbas, A. Ali, J. Li, T. T. T. Tun, and D. S. Ang, "Forming-free, self-compliance WTe_2-based conductive bridge RAM with highly uniform multilevel switching for high-density memory," *IEEE Electron Device Letters*, vol. 44, no. 2, pp. 253–256, 2023.

[7] A. Ali, Y. Abbas, H. Abbas et al., "Dependence of InGaZnO and SnO_2 thin film stacking sequence for the resistive switching characteristics of conductive bridge memory devices," *Applied Surface Science*, vol. 525, Article ID 146390, 2020.

[8] Z. Wang, M. Rao, R. Midya et al., "Threshold switching of Ag or Cu in dielectrics: materials, mechanism, and applications," *Advanced Functional Materials*, vol. 28, no. 6, Article ID 1704862, 2017.

[9] H.-M. Huang, Y. Xiao, R. Yang et al., "Implementation of dropout neuronal units based on stochastic memristive devices in neural networks with high classification accuracy," *Advanced Science*, vol. 7, no. 18, Article ID 2001842, 2020.

[10] Q. Wu, B. Dang, C. Lu et al., "Spike encoding with optic sensory neurons enable a pulse coupled neural network for ultraviolet image segmentation," *Nano Letters*, vol. 20, no. 11, pp. 8015–8023, 2020.

[11] Z. Wang, S. Joshi, S. Savel'ev et al., "Fully memristive neural networks for pattern classification with unsupervised learning," *Nature Electronics*, vol. 1, pp. 137–145, 2018.

[12] Q. Xia and J. J. Yang, "Memristive crossbar arrays for brain-inspired computing," *Nature Materials*, vol. 18, pp. 309–323, 2019.

[13] G. Zhou, Z. Wang, B. Sun et al., "Volatile and nonvolatile memristive devices for neuromorphic computing," *Advanced Electronic Materials*, vol. 8, no. 7, Article ID 2101127, 2022.

[14] M. D. Pickett, G. Medeiros-Ribeiro, and R. S. Williams, "A scalable neuristor built with Mott memristors," *Nature Materials*, vol. 12, no. 2, pp. 114–117, 2013.

[15] Y.-F. Lu, Y. Li, H. Li et al., "Low-power artificial neurons based on Ag/TiN/$HfAlO_x$/Pt threshold switching memristor for neuromorphic computing," *IEEE Electron Device Letters*, vol. 41, no. 8, pp. 1245–1248, 2020.

[16] M. Zhao, S. Wang, D. Li et al., "Silk protein based volatile threshold switching memristors for neuromorphic computing," *Advanced Electronic Materials*, vol. 8, no. 4, Article ID 2101139, 2022.

[17] A. Chen, Y. Fu, G. Ma et al., "The co-improvement of selectivity and uniformity on NbO_x-based selector by Al-doping," *IEEE Electron Device Letters*, vol. 43, no. 6, pp. 870–873, 2022.

[18] K. D. Miller and J. M. Rondinelli, "Carrier-induced metal-insulator transition in trirutile $MgTa_2O_6$," *Physical Review Materials*, vol. 6, no. 7, Article ID 075007, 2022.

[19] T. Kim, S.-H. Kim, J.-H. Park et al., "An artificial neuron using a bipolar electrochemical metallization switch and its enhanced spiking properties through filament confinement," *Advanced Electronic Materials*, vol. 7, no. 1, Article ID 2000410, 2020.

[20] Y. Li, J. Tang, B. Gao et al., "High-uniformity threshold switching HfO_2-based selectors with patterned Ag nanodots," *Advanced Science*, vol. 7, no. 22, Article ID 2002251, 2020.

[21] M. Xu, X. Mai, J. Lin et al., "Recent advances on neuromorphic devices based on chalcogenide phase-change materials," *Advanced Functional Materials*, vol. 30, no. 50, Article ID 2003419, 2020.

[22] R. Shi, Y. Chen, X. Cai et al., "Phase management in single-crystalline vanadium dioxide beams," *Nature Communications*, vol. 12, Article ID 4214, 2021.

[23] S. Kumar, R. S. Williams, and Z. Wang, "Third-order nanocircuit elements for neuromorphic engineering," *Nature*, vol. 585, pp. 518–523, 2020.

[24] C. Funck, S. Menzel, N. Aslam et al., "Multidimensional simulation of threshold switching in NbO_2 based on an electric field triggered thermal runaway model," *Advanced Electronic Materials*, vol. 2, no. 7, Article ID 1600169, 2016.

[25] D. Y. Kang, A. Rani, K. J. Yoo, and T. G. Kim, "Improved threshold switching characteristics of vanadium oxide/oxynitride-based multilayer selector in a cross-point array," *Journal of Alloys and Compounds*, vol. 922, Article ID 166192, 2022.

[26] Z. Sun, J. Zhou, and R. Ahuja, "Structure of phase change materials for data storage," *Physical Review Letters*, vol. 96, no. 5, Article ID 055507, 2006.

[27] D. Lencer, M. Salinga, B. Grabowski, T. Hickel, J. Neugebauer, and M. Wuttig, "A map for phase-change materials," *Nature Materials*, vol. 7, pp. 972–977, 2008.

[28] J. Akola and R. O. Jones, "Structure of liquid phase change material AgInSbTe from density functional/molecular dynamics simulations," *Applied Physics Letters*, vol. 94, Article ID 251905, 2009.

[29] Y. Sun, C. Song, S. Yin et al., "Design of a controllable redox-diffusive threshold switching memristor," *Advanced Electronic Materials*, vol. 6, no. 11, Article ID 2000695, 2020.

[30] S. Lee, W. Banerjee, S. Lee, C. Sung, and H. Hwang, "Improved threshold switching and endurance characteristics using controlled atomic-scale switching in a 0.5 nm thick stoichiometric HfO_2 layer," *Advanced Electronic Materials*, vol. 7, no. 2, Article ID 2000869, 2021.

[31] J. Yoo, J. Park, J. Song, S. Lim, and H. Hwang, "Field-induced nucleation in threshold switching characteristics of electrochemical metallization devices," *Applied Physics Letters*, vol. 111, Article ID 063109, 2017.

[32] Q. Hua, H. Wu, B. Gao et al., "A threshold switching selector based on highly ordered Ag nanodots for X-point memory applications," *Advanced Science*, vol. 6, no. 10, Article ID 1900024, 2019.

[33] Z. Qu, B. Zhang, C. Li et al., "A novel WO_x-based memristor with a Ti nano-island array," *Electrochimica Acta*, vol. 377, Article ID 138123, 2021.

[34] K. Tapily, J. E. Jakes, D. Gu, H. Baumgart, and A. A. Elmustafa, "Nanomechanical study of amorphous and polycrystalline ALD HfO_2 thin films," *International Journal of Surface Science and Engineering*, vol. 5, no. 2-3, pp. 193–204, 2011.

[35] T.-Y. Yu, K.-L. Lin, P.-G. Chen, and T.-H. Chou, "Structural and electronic properties of HfO_2 films on Si through H_2O_2 wet oxidation with improved thermal stability," *Surface and Interface Analysis*, vol. 54, no. 8, pp. 864–872, 2022.

[36] J. Wang, L. Li, H. Huyan, X. Pan, and S. S. Nonnenmann, "Highly uniform resistive switching in HfO_2 films embedded with ordered metal nanoisland arrays," *Advanced Functional Materials*, vol. 29, no. 25, Article ID 1808430, 2019.

[37] T. Kakiuchi, T. Matoba, D. Koyama, Y. Yamamoto, and A. Yoshigoe, "Oxidation mechanisms of hafnium overlayers deposited on an Si(111) substrate," *Langmuir*, vol. 38, no. 8, pp. 2642–2650, 2022.

[38] Y.-F. Lu, H.-Y. Li, Y. Li et al., "A high-performance Ag/TiN/HfO_x/HfO_y/HfO_x/Pt diffusive memristor for calibration-free true random number generator," *Advanced Electronic Materials*, vol. 8, no. 9, Article ID 2200202, 2022.

[39] J.-C. Lee, S.-J. Oh, M. Cho, C. S. Hwang, and R. Jung, "Chemical structure of the interface in ultrathin HfO_2/Si films," *Applied Physics Letters*, vol. 84, no. 8, pp. 1305–1307, 2004.

[40] Y.-H. Dai, Z. Chen, B. Jin, N. Li, and X.-F. Li, "Optimal migration path of Ag in HfO_2: a first principles study," *Chinese Physics B*, vol. 24, no. 7, Article ID 073101, 2015.

[41] J.-H. Park, S.-H. Kim, S.-G. Kim, K. Heo, and H.-Y. Yu, "Nitrogen-induced filament confinement technique for a highly reliable hafnium-based electrochemical metallization threshold switch and its application to flexible logic circuits," *ACS Applied Materials & Interfaces*, vol. 11, no. 9, pp. 9182–9189, 2019.

[42] G. Molas, E. Vianello, F. Dahmani et al., "Controlling oxygen vacancies in doped oxide based CBRAM for improved memory performances," in *2014 IEEE International Electron Devices Meeting*, pp. 6.1.1–6.1.4, IEEE, 2014.

[43] Z. Wang, S. Joshi, S. E. Savel'ev et al., "Memristors with diffusive dynamics as synaptic emulators for neuromorphic computing," *Nature Materials*, vol. 16, pp. 101–108, 2017.

[44] H. Sun, Q. Liu, C. Li et al., "Direct observation of conversion between threshold switching and memory switching induced by conductive filament morphology," *Advanced Functional Materials*, vol. 24, no. 36, pp. 5679–5686, 2014.

[45] I. Valov, E. Linn, S. Tappertzhofen et al., "Nanobatteries in redox-based resistive switches require extension of memristor theory," *Nature Communications*, vol. 4, Article ID 1771, 2013.

[46] R. Midya, Z. Wang, J. Zhang et al., "Anatomy of Ag/Hafnia-based selectors with 10^{10} nonlinearity," *Advanced Materials*, vol. 29, no. 12, Article ID 1604457, 2017.

[47] W. Banerjee, S. H. Kim, S. Lee, D. Lee, and H. Hwang, "An efficient approach based on tuned nanoionics to maximize memory characteristics in Ag-based devices," *Advanced Electronic Materials*, vol. 7, no. 4, Article ID 2100022, 2021.

[48] B. Song, R. Cao, H. Xu, S. Liu, H. Liu, and Q. Li, "A HfO_2/SiTe based dual-layer selector device with minor threshold voltage variation," *Nanomaterials*, vol. 9, no. 3, Article ID 408, 2019.

[49] D. P. Sahu, K. Park, J. Han, and T.-S. Yoon, "Improvement of forming-free threshold switching reliability of CeO_2-based selector device by controlling volatile filament formation behaviors," *APL Materials*, vol. 10, no. 5, Article ID 051111, 2022.